Journal of Volcanology and Geothermal Research 357 (2018) 56–67

Contents lists available at ScienceDirect

Journal of Volcanology and Geothermal Research

journal homepage: www.elsevier.com/locate/jvolgeores

Spatial and temporal patterns of deformation at the Tendaho geothermal prospect, Ethiopia

Tesfaye Temtime[a,*], Juliet Biggs[a], Elias Lewi[b], Ian Hamling[c], Tim Wright[d], Atalay Ayele[b]

[a] School of Earth Sciences, University of Bristol, BS8 1RJ Bristol, UK
[b] IGSSA, Addis Ababa University, P.O.Box 1176, Addis Ababa, Ethiopia
[c] GNS Science, PO Box 30-368, Lower Hutt 5040, New Zealand
[d] School of Earth and Environment, University of Leeds, LS2 9JT Leeds, UK

ARTICLE INFO

Article history:
Received 17 October 2017
Received in revised form 4 April 2018
Accepted 6 April 2018
Available online 12 April 2018

Keywords:
Subsidence
Afar
InSAR
Geothermal
Magmatic

ABSTRACT

Observations of ground deformation in East Africa have been fundamental for unveiling the tectonics of continental rifting, assessing the seismic and volcanic hazard to development, and identifying geothermal resources. Here we investigate the active natural and anthropogenic processes in the Tendaho Graben, Afar using Interferometric Synthetic Aperture Radar (InSAR) collected by the Envisat satellite in 2004–2010. We used the Poly-Interferometric Rate And time series Estimation (π-RATE) method to calculate displacement in satellite line-of-sight, and a least-square inversion to decompose the line-of-sight displacement into vertical and rift perpendicular components. We observe two zones of deformation: a 20 km wide circular region of subsidence located 10 km northeast of the town of Semera with a maximum displacement rate of ~5 cm/yr; and elongated zone (50 km) of subsidence in the area of the geothermal prospect, maximum rate of ~4 cm/yr. The temporal characteristics of subsidence varies between these zones, with an increase in subsidence rate observed in the circular region in August 2008. We used a Bayesian inversion to find the best fitting source models and compared this to locations of seismicity and other geophysical observations. The pattern of deformation is consistent with a combination of magmatic and geothermal processes, but there does not appear to be a direct link to a sequence of dyke intrusions during 2005–2010 at Manda Hararo graben ~60 km away, but dynamic stress changes or deep crustal flow could account for the observations.

1. Introduction

In complex tectonic settings, numerous natural and anthropogenic processes can cause surface deformation, including magmatic processes (e.g. Wright et al., 2006; Hamling et al., 2009), volcanic processes (e.g. Biggs et al., 2011; Lu et al., 2010), hydrothermal circulation (e.g. Kwoun et al., 2006; Vilardo et al., 2010; Biggs et al., 2011), fault processes (e.g. Hussain et al., 2016; Hamling et al., 2017) and water pumping from, and recharge of, water aquifers (e.g. Galloway et al., 1998; González et al., 2012). When deformation is detected and monitored, it may provide important insight into the extent, morphology, and dynamics of subsurface fluid reservoirs (e.g. Fialko and Simons, 2000; Rosen et al., 1996; Vasco et al., 2002). The deformation and its source mechanism enable us to understand the role of magmatism in continental break-up, identifying resources, and informing hazard analyses (e.g. Ebinger and Casey, 2001; Vasco et al., 2002; Ayele et al., 2015).

The area of study is the 50 km wide Tendaho graben (TG) (Kidane et al., 2003) which represents the south-eastern extension of the Red Sea rift and is the largest basin in central Afar (Fig. 1) (Acocella et al., 2008). Despite the tectonic and volcanic activity in this area, it is rapidly developing, and major infrastructure development projects include the recently-completed Tendaho Dam (Ayele et al., 2015) and the Tendaho geothermal prospect (Aquater, 1996; Gianelli et al., 1998; Battistelli et al., 2002; Didana et al., 2014). The Tendaho Dam is built on the fault scarp of Tendaho Goba'Ada Discontinuity (TGD) (Fig. 1) which is the northern end of Main Ethiopian Rift (MER) (Ayele et al., 2015).This study was initially designed to investigate the loading effects caused by the Tendaho Dam, which was known to have triggered local seismicity (Ayele et al., 2015). Although no deformation was identified associated with the dam, deformation was detected associated with the nearby geothermal prospect, and is the focus of this paper.

This study is the first to detect deformation of the Tendaho geothermal prospect, and investigates the driving mechanism and

* Corresponding author.
E-mail address: tesfaye.tessema@bristol.ac.uk (T. Temtime).

https://doi.org/10.1016/j.jvolgeores.2018.04.004

links to other regional events. Here, we use InSAR to investigate the spatial and temporal characteristics of deformation within the Tendaho geothermal prospect. We compare the time-series of the InSAR to a single GPS station located near the deformation signal. We recover rift perpendicular and vertical components from ascending and descending passes of the Envisat satellite and use simple elastic models as first order estimation to explain the source of the deformation. We examine the effect of static stress changes due to the rifting episode in the neighbouring rift segment. We compare the results to recent studies of seismicity and other geophysical observations to discuss a range of potential source mechanisms. Understanding the spatially complex pattern of surface deformation is important for unveiling the tectonics of the region, for assessing the seismic and volcanic hazard to development, and for identifying geothermal resources.

2. Tectonic and geological setting

Throughout the East African Rift (EAR) and Red Sea region, deformation is seen associated with dyke intrusions (Wright et al., 2006; Ayele et al., 2009; Hamling et al., 2009), volcanic eruptions (e.g. Xu and Jónsson, 2015), volcanic unrest (e.g. Biggs et al., 2011) and earthquakes (e.g. d'Oreye et al., 2011; Belachew et al., 2013). The Afar Depression is tectonically and volcanically active and is one of only two places on the Earth where a spreading oceanic ridge can be studied on land (Acton et al., 1991). The Red Sea, Gulf of Aden and Main Ethiopian Rifts (MER) meet to form the triple junction between the Arabian, Nubian, and Somalian plates (Fig. 1) (McClusky et al., 2010). The Afar Rift consists of 60–100 km-long NW-SE orientated magmatic spreading segments associated with volcanism and tectonic activity (Acocella et al., 2008). The recent studies of geodesy, seismicity, geophysics and geochemistry in the Afar highlight the importance of magmatism in achieving extension during continental breakup (e.g. Ebinger and Casey, 2001; Wright et al., 2006; Hamling et al., 2009; Belachew et al., 2013).

The Tendaho graben lies in central Afar, close to the triple junction (Fig. 1) and hosts normal faults, eruptive fissures, hydrothermal vents and central volcanoes. Magnetic, gravity, surface geology, geochronology and paleomagnetic studies shows that the upper crust has been extensively modified by dyking and other magmatic intrusions (Bridges et al., 2012; Lewi et al., 2015). The extension along Tendaho and Manda Hararo grabens is accommodated by dyke intrusions, and faulting (Tapponnier et al., 1990; Acocella et al., 2008), and the faults are mainly NW-SE and NNW-SSE striking (Battistelli et al., 2002). The direction of fault motion in both the Tendaho and Manda Hararo grabens are consistent with pure extension with the possibility of a small component of left lateral sheer (Acocella et al., 2008). Hydrothermal vents are found at Alalo-Bad and around Dubti (Fig. 1) (Battistelli et al., 2002; Ayele et al., 2015). In the Tendaho geothermal prospect, three deep: TD-1 (2196 m), TD-2 (1811 m) and TD-3 (1989 m) and one shallow: TD-4 (466 m) (Fig. 1) wells were drilled during the years 1993–1995 and the lithologies observed were Quaternary lacustrine and alluvial sediments and basaltic lava flows of the Afar Stratoid Series (Battistelli et al., 2002). Drilling of deep and shallow wells for geothermal exploration revealed the presence of a liquid-dominated shallow reservoir within the active hydrothermal area (Battistelli et al., 2002).

Around 60 km northwest of the Tendaho graben lies the Manda Hararo graben (MHG), which underwent a major rifting episode in 2005, associated with the emplacement of a 60 km long and up to 8 m wide dyke (Wright et al., 2006; Ayele et al., 2009). A magnitude (M_b) ~4.7 of earthquake was first reported and then a swarm of earthquakes (magnitude 4.1–5.2) were recorded which coinciding with the opening of a new 400 m long, 80 m wide volcanic vent on the eastern flank of Dabbahu volcano (e.g. Wright et al., 2006; Ayele et al., 2007, 2009; Grandin et al., 2009). A maximum horizontal opening of 8 m perpendicular to the rift, uplift of ~1.5 m on both rift flanks with respect to the far field and extended along most of the segment surface deformation was estimated from InSAR (Wright et al., 2006; Ayele et al., 2007). The observed seismicity and surface deformation were in agreement with the injection of a 60 km long dyke, between 2 and 9 km depth along the length of the segment (Wright et al., 2006; Ayele et al., 2007; Grandin et al., 2009; Hamling et al., 2009). Repeated dyke intrusions have also continued occurring during the period 2005–2010 (Hamling et al., 2010; Belachew et al., 2011; Grandin et al., 2009). The cumulative displacements from InSAR observations shows that the Ado'Ale volcanic complex at the centre of the 60 km dyke experienced continuous uplift while the Hararo volcanic centre ~35 km to the SE of Ado'Ale subsided (Pagli et al., 2014). The stress change caused by each dyke at MHG has been shown to influence the location of the subsequent dyke (Hamling et al., 2010) and we investigate the role this dyking sequence had on the Tendaho geothermal prospect.

3. InSAR observation

Interferometric Synthetic Aperture Radar (InSAR) measures ground deformation with high spatial resolution (~10 m) over a large area (100– 1000 km) using repeatedly acquired space-borne Synthetic Aperture Radar (SAR) images (e.g. Lu et al., 2003; Bürgmann et al., 2002; Simons and Rosen, 2015; Elliott et al., 2016). The phase change of an interferogram reflects surface displacement along the line-of-sight of the satellite, but is also affected by orbital errors, atmospheric delays, and noise (e.g. Bürgmann et al., 2002; Simons and Rosen, 2015).

3.1. Interferogram processing

Interferograms were produced using the JPL/Caltech ROI_PAC software (Rosen et al., 2004). Delft precise orbits were used to subtract the orbital fringe pattern (Zandbergen et al., 2003), and remove the topographic component using the 3-arcsec Shuttle Radar Topography Mission (SRTM) digital elevation model (DEM) (Farr and Kobrick, 2000). Interferograms were then filtered using a power spectrum filter (Goldstein et al., 1998), unwrapped using a branch-cut algorithm (Chen and Zebker, 2000) and manually checked and corrected for unwrapping errors. Each interferogram is geocoded to the 3 arcsec DEM (~90 m resolution).

In this study, we used 42 ascending (track-28) and 29 descending (track-278) radar images from the Envisat satellite covering the period from 2004 to 2010 (Supplementary Table 1). We processed a total of 220 interferograms, and selected a network of interferograms with small temporal (<3 months) and perpendicular baselines (<300 m) (Supplementary Fig. 1). The Envisat satellite made few acquisitions before 2006 for ascending and before 2007 for descending tracks in our study region. We excluded interferograms that suffer from loss of coherence due to 1) large perpendicular and temporal baselines, and 2) the sugarcane plantation.

We looked at interferograms from 2004 to 2007 individually and saw no significant deformation in the Tendaho geothermal prospect, despite large magnitude deformation signals associated with the Manda Hararo dyking sequence at the Ado'Ale and Hararo volcanic complexes (see Supplementary Fig. 2). Individual interferograms from 2007 to 2010 show significant deformation around the Tendaho area, and we consider only this time period in the subsequent analyses.

3.2. Rate map formation and time series analysis

Events which cause large magnitude deformation, such as large earthquakes (Bürgmann et al., 2002; ackson et al., 2006;

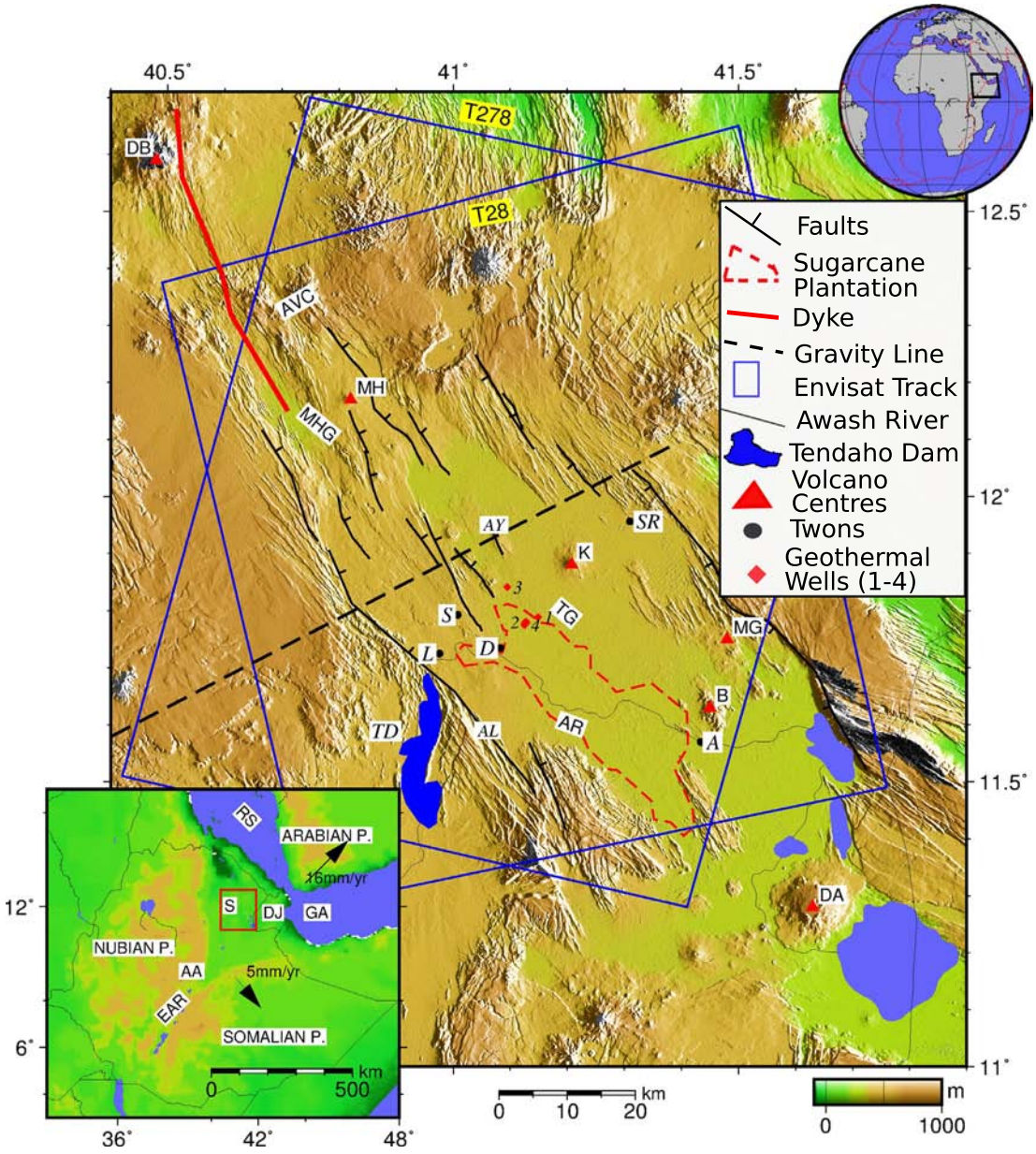

Fig. 1. Location map of central Afar. The red solid line shows the Dabbahu 2005 mega dyke intrusion (Wright et al., 2006). Red triangles show stratovolcanoes (AY: Alayta, DB: Dabbahu, MH: Manda Hararo, K: Kurub, MG: Manda Gorgori, B: Borawli, DA: Dama Ali) (Global Volcanism Program, 2013). AL: Alalo-Bad geyser. The black dashed line shows gravity (Lewi et al., 2015) and MT profiles (Johnson et al., 2015). MHG: Manda Hararo graben, AVC: Ado Ale Volcanic Complex, TG: Tendaho graben, TD: Tendaho Dam, AR: Awash River. Towns: S: Semera, D: Dubti, L: Logia, A: Asaita, SR: Serdo. Inset map shows the Nubian, Arabian and Somalian plates. The velocity vectors are after McClusky et al. (2010). The red box shows the Afar depression. Acronyms: AA: Addis Ababa, S: Semera, DJ: Djibouti, RS: Red Sea, GA: Gulf of Aden. The topographic map is generated from SRTM DEM data and ETOPO (inset map). (For interpretation of the references to colour in this figure legend, the reader is referred to the web version of this article.)

Wright et al., 2003) and dyke intrusions (Wright et al., 2006; Hamling et al., 2009) can be detected using images acquired before and after the event to form a single interferogram. However, studies of small magnitude deformation require multiple interferograms that cover long periods of time so that the deformation signal can be isolated from the noise. Many multi-interferogram methods exist to mitigate unwanted signals and reduce noise levels. For example, the time series of one-dimensional line-of-sight deformation can be computed using the Small Baseline Subset algorithm (SBAS) (Berardino et al., 2002; Lanari et al., 2007; Samsonov et al., 2011), the multi-interferogram method (π-RATE) (Biggs et al., 2007; Wang and Wright, 2012) and persistent scatterer and small baseline approaches (e.g. StaMPS) (Hooper, 2008).

We follow here the multi-interferogram method of Biggs et al. (2007), Elliott et al. (2008), and Wang et al. (2009) to produce rate maps using π-RATE (Poly Interferogram Rate And Time Series Estimator) (Wang, 2012). π-RATE is an open source package of MATLAB codes designed to estimate the linear displacement rate map, time series, and their associated uncertainties using a set of geocoded interferograms (Biggs et al., 2007; Elliott et al., 2008; Wang et al., 2009). We averaged 10 geocoded neighbouring pixels to give a resolution of ~900 m, to improve the signal to noise ratio. A pixel-wise approach is employed in π-RATE to calculate deformation rates at pixels that are coherent at least in 5 interferograms. The time series of cumulative displacements, average velocities and their associated uncertainties are obtained for each pass. The detailed algorithm and

processing steps are described in Biggs et al. (2007), Elliott et al. (2008), and Wang et al. (2012) and a brief description follows.

From a network of geocoded unwrapped interferograms, non-redundant observations are selected for the estimation of time series and a linear rate map. A minimum spanning tree (MST) algorithm is adopted to select non-redundant interferograms and increase the coverage of the rate map. All interferograms are referenced to a reference point that is assumed to be stable on Nubian plate at the southwest part of the scene ('X' sign in Fig. 2). To account for any residual orbital errors (or long wavelength atmospheric effect), we calculate and remove the best fitting quadratic plane for each interferogram based on a network approach (Biggs et al., 2007). DEM errors are estimated and removed based on the baseline information of each interferogram.

Atmospheric artefacts due to delay of the signal in the ionosphere and troposphere can have a significant effect (e.g. Hanssen, 2001). For C-band data, the ionospheric delay can usually be ignored within a scale of 50 km (Hanssen, 2001). The tropospheric delay can be categorised into a vertical stratified component and a turbulent component (Hanssen, 2001; Massonnet and Feigl, 1998; Jolivet et al., 2014). The stratified tropospheric delay, which is a function of height difference, can be estimated empirically using a linear function of the SRTM DEM (Elliott et al., 2008) or a power law correction method that accounts for spatial variability in atmospheric properties (Bekaert et al., 2015).

In regions like central Afar, where the topography is relatively flat (300 m–800 m), the stratified contribution is small (<7 mm) (Hanssen, 2001; Massonnet and Feigl, 1998; Parker et al., 2015). In these circumstances, tropospheric artefacts are best estimated using Atmospheric Phase Screening (APS), which consists of two steps: a temporal high-pass filter followed by a low-pass spatial filter similar to Ferretti et al. (2001). We used a Gaussian temporal filter with a 1σ of 0.5 years to observe long-term, steady state velocity and a Butherworth spatial filter based on the wavelength from variance-covariance matrix estimated using a best fit 1-D covariance function (Hanssen, 2001). Before estimating the final time series analysis, the residual APS and error due to decorrelation and thermal noise is removed by further smoothing in time based on a smoothing factor from a trade-off curve between weighted misfit and solution roughness (Supplementary Fig. 4). The output rate maps show the average velocity along the line-of-sight. The temporal resolution of the time series is dictated by the satellite acquisition strategy determined by the European Space Agency.

3.3. Spatial characteristics of deformation

We first estimate the line-of-sight linear rate maps and their uncertainties for ascending and descending tracks independently. In Fig. 2, the blue colour shows range decrease (i.e. motion towards the satellite) and the red colour shows range increase (i.e. motion away from the satellite). The deformation at Ado'Ale volcanic complex (AVC) and Hararo volcano (Fig. 2a and b) are due to the mega dyke intrusion which is started in 2005 and successive dyke intrusions up to 2010. These deformation events are discussed in detail in Wright et al. (2006), Ayele et al. (2007, 2009), Hamling et al. (2010, 2014), and Grandin et al. (2009). Here, we focus on the smaller magnitude deformation in the Tendaho graben (Fig. 2c and d), which is indicated by a red box in Fig. 2a and b.

Both ascending and descending rate maps show a circular region of deformation at the NE of the town of Semera and a narrow elongated deformation pattern along the NW-SE Tendaho graben. The circular deformation has a diameter of 20 km and ~50 mm/yr line-of-sight average rate of deformation. Both tracks show range increase in the line-of-sight of the satellite (Fig. 2), which suggests the deformation is mostly subsidence. The narrow elongated deformation is spatially highly variable with the average rate of deformation being about 30–50 mm/yr. The spatially variable pattern of deformation is similar to that observed at other geothermal fields, for example, Coso, California (e.g. Fialko and Simons, 2000) and Brady, Navada (e.g. Shevenell et al., 2012; Ali et al., 2016) and likely reflects the influence of minor faults or fractures in the system. In the sugarcane plantation, the estimated error is <10 mm/yr, while elsewhere it is <1 mm/yr (Supplementary Fig. 3c and d). The change is surface cover in the sugarcane plantation region increase the error. The network approach and stacking implemented in π-RATE, enables us to recover the average deformation from interferograms with better coherence.

We make profiles perpendicular to the rift axis to investigate the spatial characteristic of deformation across the deforming region (Fig. 3). Profile P1 is aligned with previously-published profiles of gravity (Lewi et al., 2015), magnetics (Bridges et al., 2012) and magnetotellurics (Johnson et al., 2015) and passes just to the north of the observed deformation (see Section 1). Along this profile, we observe maximum 10 to 15 mm/yr range increase along the line-of-sight. Profile P2 located 8 km south east from P1, crosses the centre of the circular deforming region and passes through a Quaternary lava flow (Acocella et al., 2008), that covers the northern part of town of Semera. This profile shows subsidence of <50 mm/yr at the centre. Profile P3 passes through the geothermal field, including the deep geothermal wells and magnetotelluric profiles (Didana et al., 2014) and profile P4 lies 13 km further southeast along the rift. Both these profiles show a ~15 km wide zone of deformation at the rift axis with 20 to 40 mm/yr of subsidence.

3.4. Temporal characteristics of deformation

Next, we investigate the temporal variations in deformation along the rift axis (Fig. 4), using time series analysis of pixels, each pixel (~900 m resolution) with low magnitude error close to the point of maximum deformation. Points A, B, C, D and E are pixels located at the Hararo magmatic centre, a point northeast of Semera town, the DASM continuous GPS station, the Tendaho geothermal wells, and a point to the southeast of Tendaho respectively (Fig. 2b). A to E are for descending images and F to J are for ascending images. For each point, we compare the time series with the time of dyke intrusions (the vertical lines in Fig. 4) in the neighbouring Manda Hararo segment to investigate the effect of a static (immediate) stress change due to opening/unclamping of the dykes. We convert the three dimensional GPS daily solution at site DASM in to the line-of-sight of the satellite and compare the trend with the InSAR time series (Fig. 4). The InSAR time series shows cumulative displacement relative to the first date of the image used. In order to align the InSAR time series with the GPS time series, we add a constant shift to the InSAR time series.

Table 1 summarises the best-fit linear deformation rates. Pixel A (Hararo), D (Geothermal Wells) and E (SE Semera) (Fig. 4) show subsidence throughout the observation time period both in ascending and descending images. Pixel B, which is ~30 km away from pixel A, is located at the centre of the circular subsidence and Pixel C (DASM) at periphery of the deformation show similar temporal variations, and the time series can be divided into two distinct periods: (1) before August 2008, where line-of-sight deformation occurred at a rate of 21 mm/yr (descending) and 11 mm/yr (ascending) (2) following August 2008 further deformation occurred at a rate of ~54 mm/yr (descending) and 65 mm/yr (ascending) (Table 1). We compare the InSAR time series (red in Fig. 4) with the GPS time series converted to the line-of-sight of the satellite (grey in Fig. 4) at Semera (DASM) and both demonstrate similar temporal patterns. The temporal pattern at points B and C are different from A, D and F, which suggests a different source mechanism, and a change in process around August 2008.

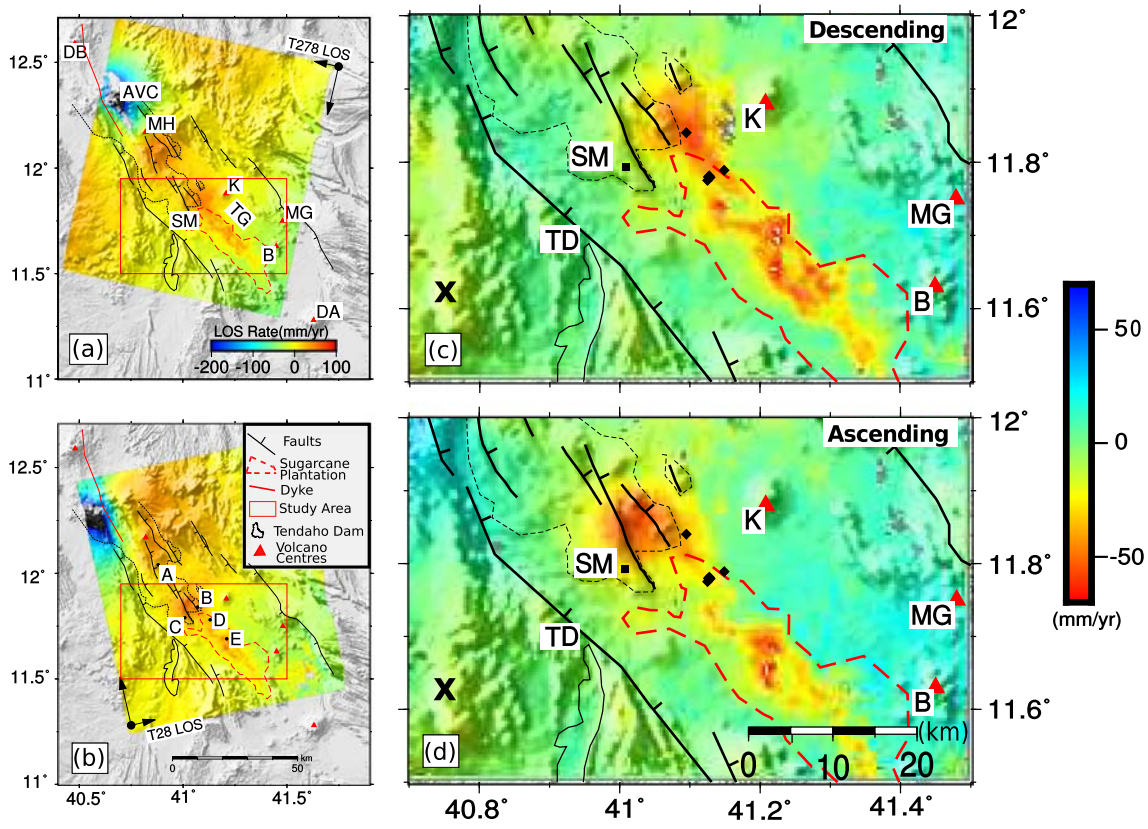

Fig. 2. Line-of-sight (LOS) average rate map of central Afar between 2007 and 2010. (a) Descending and (b) ascending tracks cover DMH and Tendaho. Blue is range decrease and red is range increase. Pixels A, B, C (DASM), D, and E in (b) are points where time series is compared (Fig. 4). The red rectangular box in (a) and (b) is the study area. (c) and (d) are descending and ascending scene over Tendaho rift. 'X' is reference pixel assumed to be stable on the Nubian plate. Other acronyms are described in Fig. 1. (For interpretation of the references to colour in this figure legend, the reader is referred to the web version of this article.)

3.5. Vertical and horizontal deformations

Multi-interferogram methods such as π-RATE only consider one-dimensional displacement in the satellite line of sight and often the three-component displacement field is more informative. Radar satellites available for interferometry are in near-polar orbits and are side-looking, so interferograms are mostly sensitive to vertical and east-west motion, and only weakly sensitive to north-south velocities (Wang and Wright, 2012; Pagli et al., 2014). However, with more than one viewing geometry, and suitable assumptions, it is possible to separate horizontal and vertical contributions to the deformation. In this case, we assume that there is no deformation parallel to the rift axis (e.g. Hamling et al., 2014).

The vertical and horizontal components of deformation can be decomposed from ascending and descending geometries using the least square inversion technique of Wright et al. (2003) and Hamling et al. (2014). The limitations of this method are as follows: 1) the two components of the displacement field can be separated only in the overlapping regions, 2) assumptions has to be made about the orientation of deformation, for example, there is no north-south (rift parallel) motion. In our case, there is complete overlap of the ascending and descending tracks covering the Tendaho geothermal prospect region, and the orientation of the Tendaho rift axis is determined from structural and geophysical methods (Acocella et al., 2008; Lewi et al., 2015). Therefore, it is possible to a certain degree to retrieve the vertical and horizontal components of the deformation by combining the tracks using certain assumptions (e.g. Wright et al., 2003; Hamling et al., 2014). We assume here there is no motion parallel to the Tendaho rift axis and solve for the rift perpendicular and vertical components using a least square inversion technique (e.g. Wright et al., 2003; Hamling et al., 2014). Any rift-parallel motion associated with tectonic motion is likely to be at least an order of magnitude slower, and can be neglected in these calculations. We use the viewing geometry of both ascending and descending passes to calculate the line-of-sight velocity vector for each pixel.

The vertical (u_z) and rift perpendicular ($u_\perp$) components can be determined by solving Eq. (1) using a least squares inversion for each pixel.

$$\begin{bmatrix} \cos\theta_s l_{xd} + \sin\theta_s l_{yd} & l_{zd} \\ \cos\theta_s l_{xa} + \sin\theta_s l_{ya} & l_{za} \end{bmatrix} \begin{bmatrix} u_\perp \\ u_z \end{bmatrix} = \begin{bmatrix} r_d \\ r_a \end{bmatrix} \quad (1)$$

where l_x, l_y and l_z are the three components of the unit vector pointing from the ground to the satellite for the ascending ($_a$) and descending ($_d$) passes, $u_\perp$ and u_z are the vertical and rift perpendicular components of the displacement respectively and r is the range change measured by the satellite. $\theta_s = 35^\circ$ is the angle between the rift perpendicular vector and the north.

We are able to recover the rift perpendicular and vertical rate of displacement using Eq. (1). To the northeast of town of Semera, the circular region of deformation, shows a significant localised horizontal closing rate (~60 mm/yr) (Fig. 5a) and the vertical component (Fig. 5b) shows subsidence (~50 mm/yr) consistent with a deflating body. The assumption we made regarding the absence of rift parallel motion, is not ideal for concentric deformation where the north-south component of the displacement maps into apparent vertical motion.

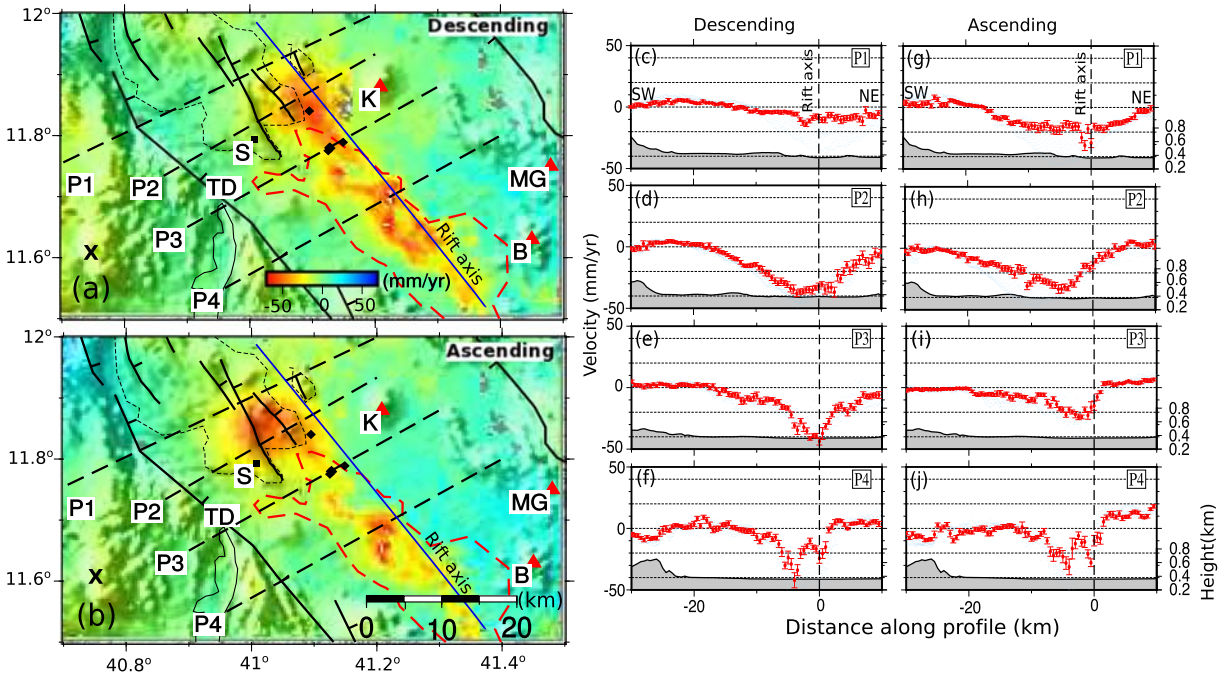

Fig. 3. Average line-of-sight rate map of the area. (a) and (b) are line-of-sight rate maps of descending and ascending passes respectively. P1, P2, P3 and P4 are the profiles across the deformation signal (c)–(f) for descending and (g)–(j) for ascending passes. Vertical broken line on the profile plots shows the inferred rift axes (Acocella et al., 2008; Lewi et al., 2015). The rate maps with associated error plots can be obtained in Supplementary Fig. 3. The black dots within the deformation area are locations of the deep geothermal wells (Battistelli et al., 2002). Other acronyms are described in Fig. 1.

In the elongated region of deformation, rift perpendicular deformation shows variable eastward motion at rate of 30 mm/yr to 70 mm/yr and localised westward motion at a rate of 50 mm/yr to 60 mm/yr. The vertical shows variable subsidence rate of 30 mm/yr to 60 mm/yr. The variable deformation pattern extends over the elongated region of deformation where the majority of the Tendaho geothermal wells were drilled and geothermal surface manifestations have been observed (e.g. Battistelli et al., 2002). As a result of spatially complex deformation with patches of localised subsidence, east-west motion is not recovered well.

We use the same profiles as in Section 3.3. to make profiles across the deforming regions. Profiles P1 and P2 show more horizontal motion than profiles P3 and P4. The profiles of vertical displacement show a broad deformation area at profiles P1 and P2 (~25 km) and a narrower deformation area at profiles P3 (~15 km) and P4 (~10 km). The width of the deforming area becomes narrower going SE along the rift axis. The vertical component shows similar patters to the line-of-sight profiles in Section 3.3, but decomposing in to vertical and rift-perpendicular enables us to see that there is a significant horizontal motion with comparable order of magnitude to the vertical component.

4. Geodetic source modelling

The spatial and temporal pattern of deformation demonstrates two sources of deformation at the Tendaho geothermal prospect with two distinct spatial and temporal patterns. To characterise the source of deformation at the Tendaho geothermal prospect, we use simple analytic solutions in an elastic half-space, including a Mogi model (Mogi, 1958) and horizontal rectangular sill (Okada, 1985).These analytical models are widely used to calculate surface deformation related to the pressurisation of a magma chamber or the opening of a sill/dyke (e.g. Hamling et al., 2014; Sanderson et al., 2010; Stiros et al., 2010; Grandin et al., 2010) but do not consider, for example, topography, gravity, non-uniformity of the elastic properties (e.g. Young's modulus, Poisson's ratio), vertical layering, time-varying material properties and lateral inhomogeneity (Cayol and Cornet, 1998; Masterlark, 2007; Gottsmann et al., 2006b; Manconi et al., 2007; Lisowski, 2007). Nevertheless, they provide a good first order approximation of the geometry of the deformation source.

We use an open source Geodetic Bayesian Inversion Software (GBIS) (http://comet.nerc.ac.uk/gbis) to estimate deformation source parameters from the ascending and descending average rate of surface deformation. The software implements a Markov Chain Monte Carlo algorithm, incorporating the Metropolis-Hasting algorithm (Mosegaard and Tarantola, 1995; Hooper et al., 2013; González et al., 2015) to estimate the posterior probability distribution for different model parameters based on a priori values of the source model considered (González et al., 2015). The optimal solution and its uncertainty is determined for each model parameter based on the estimated Gaussian distribution of the model parameter. Here, we solve for the locations, depth, and volume estimate of point source representing the circular region of deformation; and location, depth, strike, opening and dimensions of the sill representing the elongated region to the SE.

In Fig. 6, we show the comparison between observed rate of displacements, model prediction, and residuals from each track, with the corresponding model parameters in Table 2. The inferred depth of the Mogi point source is ~12 ± 0.6 km and for the horizontal sill is ~3 ± 0.5 km. The model matches the observation well in the circular region of deformation. Heterogeneity is evident in the spatial variation at the elongated region of subsidence as described in Section 3.3. Although this simple model cannot accurately reproduce the deformation pattern, it matches the overall extent and magnitude well. The heterogeneous pattern of deformation may reflect the influence of minor faults or fractures within the region (e.g. Fialko and Simons, 2000; Shevenell et al., 2012; Ali et al., 2016).

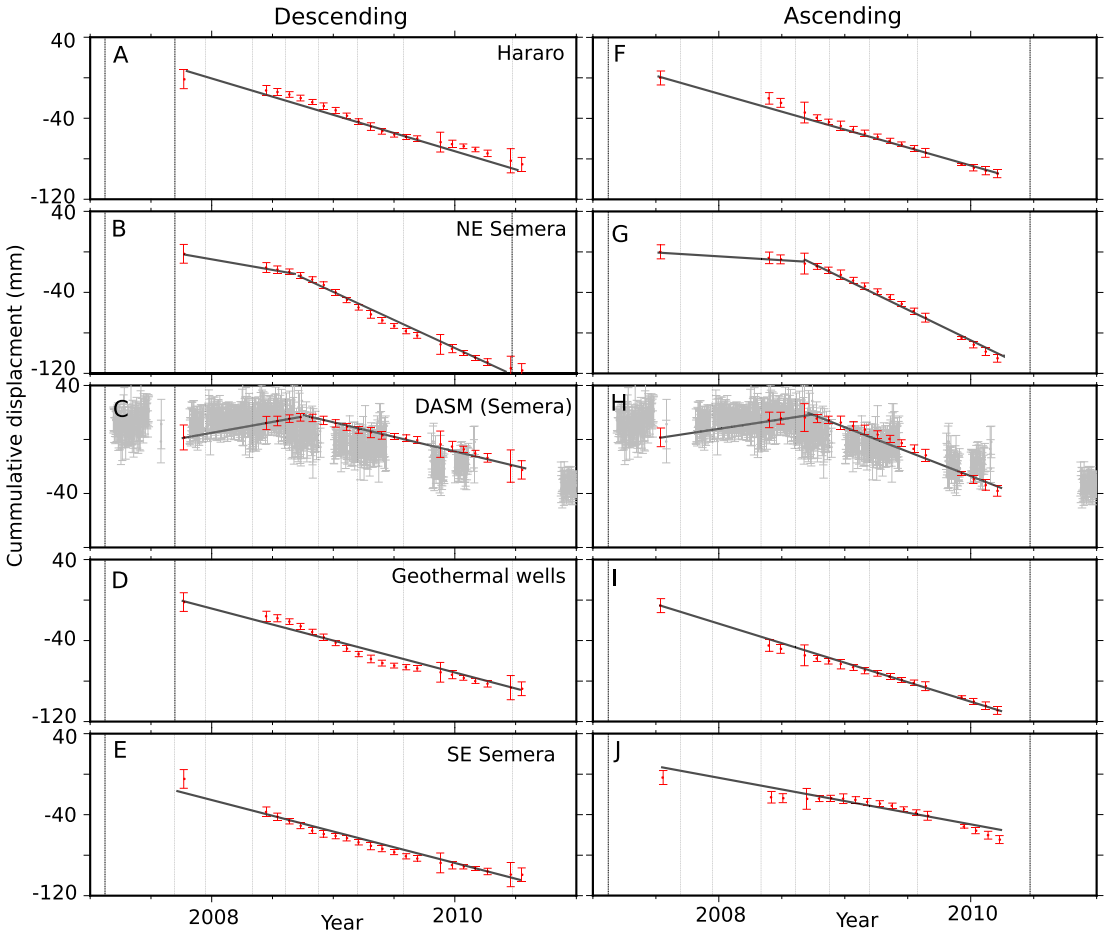

Fig. 4. Cumulative line-of-sight displacement, pixels taken along the rift axis centre. (A) Hararo volcanic centre, (B) circular deformation at NE of the town of Semera, C (DASM) is in the town of Semera where a continuous GPS station exists (grey is GPS time series and red is InSAR time series), (D) Tendaho geothermal wells, and (E) pixel at 13 km southeast from D, the black vertical lines are dates of the dyke intrusions. We added a constant value to the InSAR time series to match the GPS measurement, because the InSAR measurement is a relative measurement only. See Fig. 2b for the locations of points. (For interpretation of the references to colour in this figure legend, the reader is referred to the web version of this article.)

5. Discussion

5.1. Deformation sources

Within the Tendaho graben, we observe a complex region of deformation composed of circular region of deflation connected to an elongated zone of subsidence along the Tendaho geothermal prospect. The magnitude of the signal in both deformation regions is much smaller than measured in the Manda Hararo magmatic segment, but is comparable to that observed at silicic volcanoes and geothermal systems within the Main Ethiopian Rift (e.g. Biggs et al., 2011; Hutchison et al., 2015) and in the Kenyan Rift (Biggs et al., 2009, 2016a; Robertson et al., 2016).

The deformation patterns indicate at least two separate sources of deformation: (1) a deflating point source and (2) a closing sill like body with estimated depths of 12 ± 0.6 km and 3 ± 0.5 km respectively. The deflating point source corresponds to positive magnetic and gravity anomalies and a region of high electrical conductivity

Table 1
Time series of selected pixels. Pre- and post-August 2008 trend change.

		Pre-August 2008			Post-August 2008		
	Pixels	Slope (mm/yr)	RMSE (mm)	R^2	Slope (mm/yr)	RMSE (mm)	R^2
Descending	A (Hararo)	−33	4	0.97	−33	4	0.97
	B (NE Semera)	−21	1	0.98	−54	5	0.98
	C (DASM)	16	1	0.99	−20	2	0.98
	D (Geothermal Wells)	−35	5	0.96	−35	5	0.96
	E (SE Semera)	−32	5	0.96	−32	5	0.96
Ascending	A (Hararo)	−38	3	0.98	−38	3	0.98
	B (NE Semera)	−11	2	0.85	−65	2	0.99
	C (DASM)	12	2	0.91	−39	3	0.98
	D (Geothermal Wells)	−36	2	0.99	−36	2	0.99
	E (SE Semera)	−22	5	0.88	−22	5	0.88

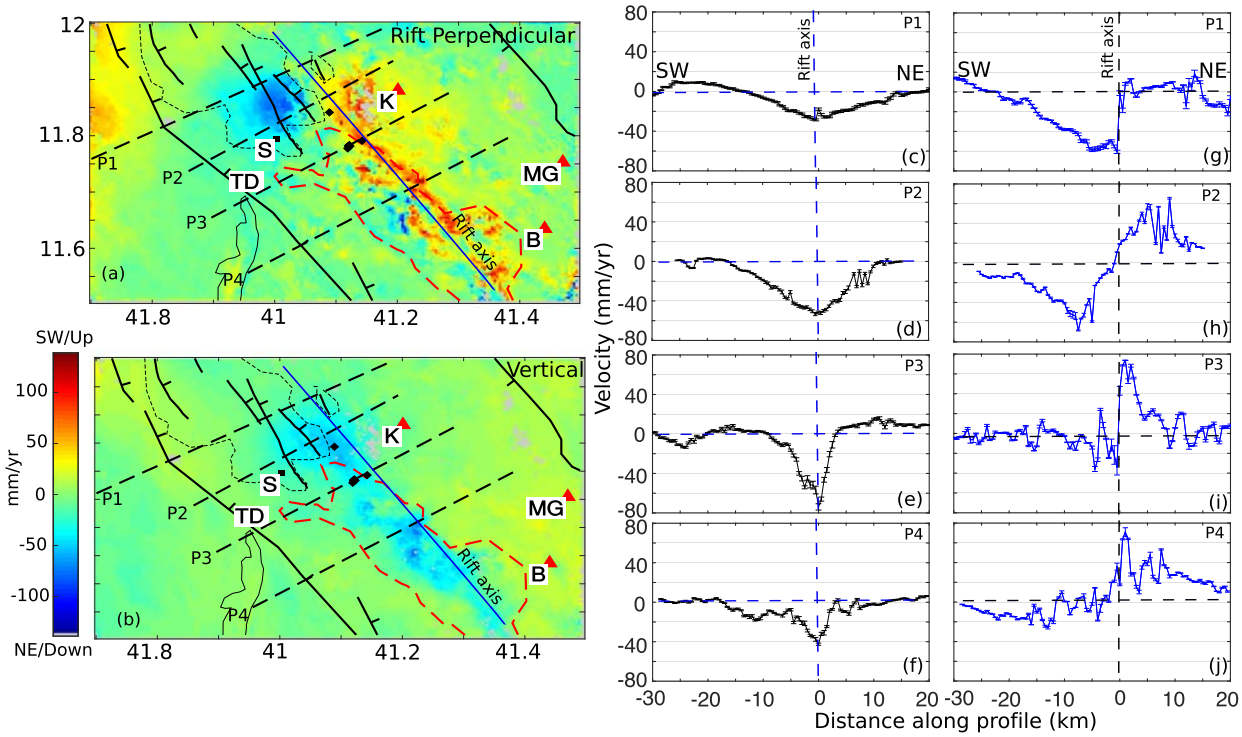

Fig. 5. Vertical and rift perpendicular rate map. (a) Rift perpendicular, blue shows to the NE and red shows SW directions, (b) is vertical, blue shows down and red shows up, (c)–(f) are vertical profiles, (g)–(j) are rift perpendicular profiles. The P1 to P4 are profiles, start at SW and end at NE across the rift. All acronyms and features are on Figs. 1 and 2. (For interpretation of the references to colour in this figure legend, the reader is referred to the web version of this article.)

(Bridges et al., 2012; Lewi et al., 2015; Johnson et al., 2015) with estimate depths of 8–15 km. These observations suggest the deformation here is caused by a pressure or volume decrease within a deep magma chamber or a zone of partial melt. A well drilled in this region (TD-3) exhibits cooler temperature of 170 °C at 1 km, and mineralogy and fluid inclusions indicate a cooling process has occurred in the shallow layers characterised by low permeability and self-sealing (Gianelli et al., 1998).

The elongated region of subsidence corresponds to the Tendaho geothermal field, where geothermal exploration wells (TD-1, TD-2, and TD-4) revealed the presence of a liquid-dominated shallow hydrothermal reservoir. The reservoir is characterised by a temperature distribution close to a boiling-point-for-depth (BPD) curve down to about 500 m, with temperature of 270 °C at the wells bottom depth of ~2 km. Mineralogy and fluid inclusions at TD-2 and TD-4 suggest this area is in the stable upflow zone, whereas at TD-1,

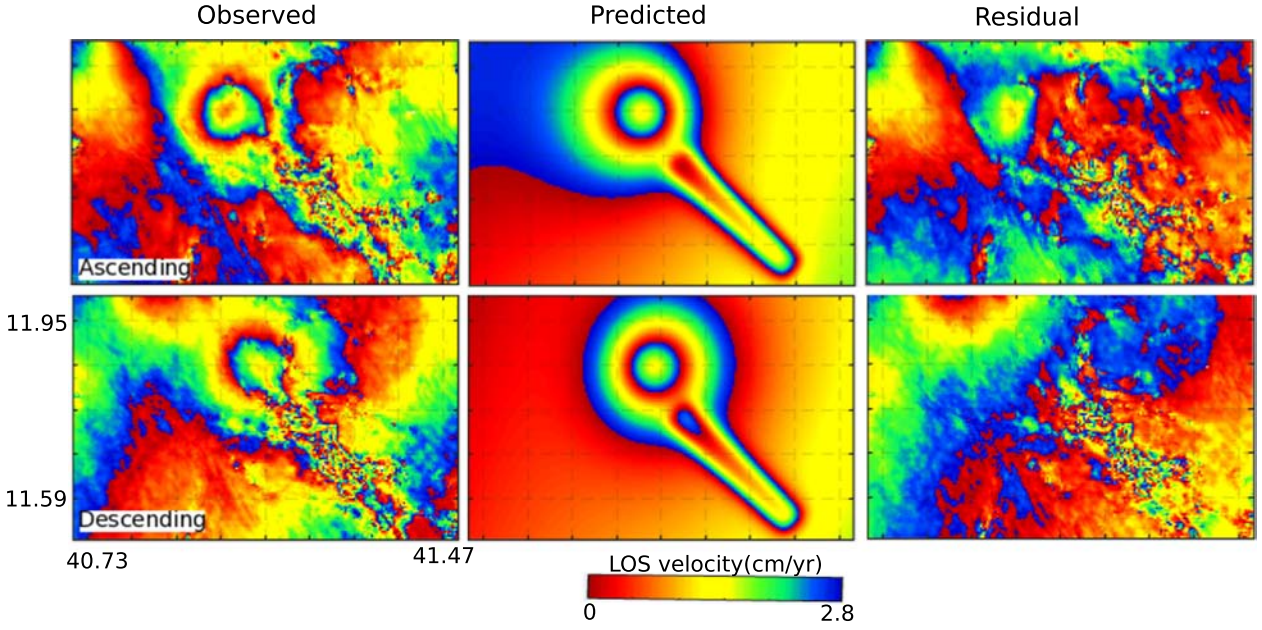

Fig. 6. Bayesian inversion modelling results of descending and ascending average rate map. (left column) Line-of-sight average rate map, (middle column) best-fitting models, and (right column) residual maps. The data covers the period 2007–2010.

Table 2
Estimated best-fitting optimal parameters for the presented models.

Model	Length (km)	Width (km)	Depth (km)	Strike (°)	Latitude (°)	Longitude (°)	Volume (km^3/yr)	Opening (cm/yr)
Mogi	–	–	12 ± 0.6	–	11.856	41.072	-0.03 ± 0.006	–
Sill	36 ± 0.6	6 ± 0.2	3 ± 0.5	314 ± 1	11.669	41.267	–	-4 ± 0.8

there is evidence of a recent heating event (Battistelli et al., 2002; Gianelli et al., 1998). The magnetotelluric data demonstrate that an upper crustal zone of fractures and partial melt extends for depths of 1–15 km with a maximum width of 15 km (Didana et al., 2014). S-wave splitting measurements support that the presence of shallow NW-SE trending cracks (and/or faults) affecting the Tendaho graben (Keir et al., 2011). The shallow elongated deformation is likely associated with the response of the geothermal system to changes in the stress or thermal regime associated with magma withdrawal from the nearby deep reservoir.

5.2. Local seismicity

Three separate seismic arrays have reported seismic activity in the area over the past 40 years (Fig. 7). These arrays are as follows: 1) in the 1970s to study local seismicity (Rigden, 1981); 2) in the 1990s, for geothermal energy exploration (Aquater, 1996; Gresta et al., 1997), and 3) from 2007 to 2011 following the September 2005 mega dyke intrusion at Manda Hararo (Ayele et al., 2015, 2009; Belachew et al., 2013). The epicentre locations correlate well with the deflating point source with depths of 2–10 km, shallowest at the centre of the deformation. Minor seismicity was also recorded at Alalo-Bad geyser (Fig. 1), by the Tendaho dam, and may reflect stress changes caused by the dam loading (Ayele et al., 2015). These observations demonstrate the region experiences frequent seismicity and the deformation we observe may simply be the latest in an ongoing sequence.

Localised seismicity was also observed on the northern side of Kurub volcano during 1990s and 2007–2011 surveys (Fig. 7). Belachew et al. (2011) suggest that the later activity has been attributed to stress transfer from the dyke intrusions in the Dabbahu Manda Hararo graben segment 60 km away. Neither Kurub volcano, nor the other volcanoes of the Tendaho graben, Manda Gorgori and Borawli (Global Volcanism Program, 2013), show significant deformation during this time.

5.3. Comparison to other geothermal fields

Though the Tendaho geothermal field is at the exploration stage, it shows deformation associated with sub-surface magmatic and hydrothermal processes. In operational geothermal fields, deformation is associated with production-induced subsidence and likely as a result of cooling and/or depletion of the geothermal reservoir (e.g. Coso geothermal field, in California (Vasco et al., 2013)). In geothermal prospect areas, geodetic observations reveal that active magmatic and/or hydrothermal systems show episodic uplift and subsidence. For example, the Main Ethiopian Rift shows pulses of deformation have occurred at four volcanic edifices (Aluto, Corbetti, Bora and Haledebi) (Biggs et al., 2011). The Aluto geothermal field episodic deformation has explained by magma-driven uplift amplified by increased activity in the hydrothermal field, followed by subsidence associated with the hydrothermal field alone (Biggs et al., 2011; Hutchison et al., 2016). The geothermal systems in Kenyan rift show also such episodic nature of deformation with a pulse of magma arriving in the shallow crust or change in the hydrothermal system triggered by magmatic pulses in the mid- or lower crust (Biggs et al., 2009, 2016b).

A period of rapid inflation and deflation observed by gravity and geodetic observations at Campi Flegrei, Italy, suggests volume change in both magmatic and hydrothermal systems (e.g. Gottsmann et al., 2006a; Lanari et al., 2004; Gaudio et al., 2010). One suggestion is that overpressure of magma or fluids of magmatic origin beneath an impermeable barrier causes uplift whereas when a major breach of this zone occurs brine and gases migrated to the brittle, lower pressure, colder aquifer which leads to efficient discharge of fluids by lateral migration resulting in subsidence (Battaglia et al., 2006). InSAR and GPS observation at the Taupo Volcanic Zone, New Zealand show the majority of the observed subsidence is a result of cooling and subsequent contraction of magma within the shallow crust (Hamling et al., 2015).

Thus, magmatic and/or hydrothermal processes at geothermal prospects produce complex patterns of deformation and better observation, analysis and modelling is required to fully understand the system at Tendaho. Deformation at the Tendaho geothermal field is consistent with other geothermal prospecting regions and might give insight to understand mechanism of subsurface processes during exploration and future implications for hazards during geothermal energy production.

5.4. Regional influences

We investigate the regional effects caused by the dyking sequence from 2005 to 2010 in the Manda Hararo graben on the Tendaho geothermal field. We initially use the data and method described in Hamling et al. (2010) to consider static stress changes and then consider other possible connections such as deep crustal flow or dynamic triggering.

Stress changes on the order of megapascals are sufficient to open pre-existing cracks and cause active magma migration (e.g. Walter, 2007). We calculate full tensor of stress change for the Manda Hararo sequence at depths from 10 km to 15 km at 1 km steps and decomposed into isotropic (hydrostatic) and a deviatoric components. The change in isotropic stress (mean normal stress) at Tendaho geothermal prospect ranges from 0.2 to 1.6 kPa, except for the September 2005 mega dyke, for which we estimate a maximum stress change of 16 kPa. These stress changes are on the same order of magnitude as stress variations due to Earth tides (Lockner and Beeler, 1999, and references therein) so are considered insufficient to open pre-existing cracks and allow magma migration (Walter, 2007; Hamling et al., 2010, 2014). Hence, the deformation at the geothermal prospect area is unlikely to be directly caused by the stress change during dyke intrusions at Dabbahu Manda Hararo.

Geothermal regions are susceptible to local earthquakes triggered by regional and remote earthquakes (Aiken and Peng, 2014) suggesting critically stressed faults and the presence of fluids in geothermal regions are favourable conditions for triggering micro earthquakes from distant, large amplitude earthquakes. The 2010 M_w 8.8 Maule earthquake, Chile, induced a subsidence at southern Andes volcanoes as a result of static stress change that causes the release of hydrothermal fluids, increased streamflow and ground deformation (Pritchard et al., 2013). Similarly, the 2011 M_w 9.0 Tohuku earthquake, Japan, triggered a volcanic subsidence regions located between 150 and 200 km from the rapture area (e.g. Takada and Fukushima, 2014). The earthquakes associated with the Manda Hararo dyking sequence are magnitude (M_L) <5.6 (Ayele et al., 2007; Belachew et al., 2013)

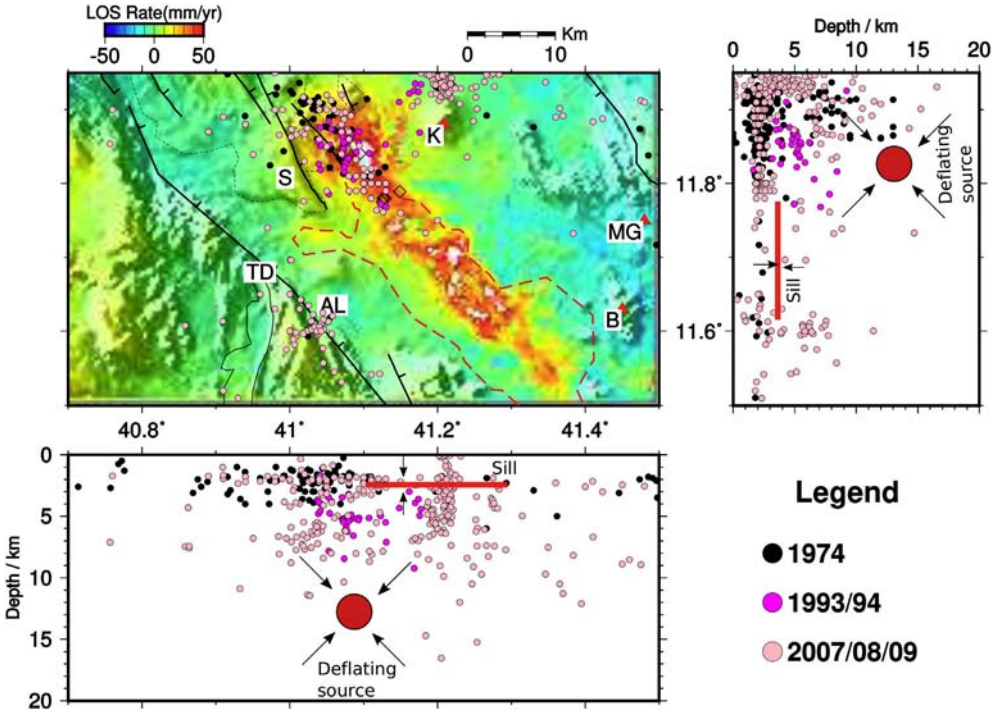

Fig. 7. Local seismicity of Tendaho geothermal prospect. The black, purple and pink circles show 1974 (Rigden, 1981), 1993/1994 (Gresta et al., 1997) and 2007/2008/2009 (Ayele et al., 2015) seismic networks respectively. The depth of the deflating source and a closing sill are from the Bayesian inversion. AL: Alalo-Bad geyser.

and is unlikely that dynamic stress from regional earthquakes significantly perturb the Tendaho magmatic and geothermal systems, but the possibility cannot be discounted.

Hararo volcano, 30 km northwest from the Tendaho geothermal prospect shows a linear subsidence for the time period of 2007–2010 (Hamling et al., 2009; Grandin et al., 2010; Pagli et al., 2014) which has been attributed to a deflating magma chamber at 17 km depth (Grandin et al., 2010). Pagli et al. (2014) compared InSAR time series at Ado'Ale and Hararo magmatic systems concluding that the velocity changes at Hararo are coeval with an uplift in Ado'Ale. They suggested that the signals are likely caused by magma flow at deep crustal level than related to dyke intrusion processes occurring at shallow depth. Thus, although the circular deformation at Tendaho has a different temporal characteristics, it might also be associated with this deep crustal magma flow considering the spatial proximity.

6. Conclusion

Here we present geodetic observations at a complex region of deformation in the Tendaho geothermal prospect, Afar: a 20 km wide region associated with a deep (12 ± 0.6 km) point source located 10 km northeast of the town of Semera with a maximum displacement rate of ~5 cm/yr; and a shallow (3 ± 0.5 km), elongated zone (50 km) of subsidence in the area of the geothermal prospect, maximum rate of ~4 cm/yr. The pattern of deformation is consistent with deflation of a magma source or a zone of partial melt at 12 km depth located close to the town of Semara, with subsidence in the NW-SE elongated hydrothermal system at a depth of 3 km. The static stress change during the dyking episode at Manda Hararo magmatic segment is too small to directly trigger the magma movement, but the deformation might be due to deep crustal magma flow or linked to shallow hydrothermal fluid circulation. The area is a major import-export hub, has towns with large population, and new infrastructure such as Tendaho dam and sugar factory. The results have implications for both the ongoing geothermal exploration and the potential hazard to development. Observation of such a deformation improves our understanding of the complex extent and dynamics of geothermal prospect areas and may be key to unlocking resources.

Acknowledgments

TT is supported by Michael Dreyfus PhD Alumni Scholarship, JB is supported by the NERC COMET+ and NERC RiftVolc Grant NE/I01372X/1. TT would like to thank IGSSA, Addis Ababa University, Addis Ababa, Ethiopia and the STEP programme, International Centre for Theoretical Physics (ICTP), Trieste, Italy for their support during the initial stage of the work. We thank the Editor and the two anonymous reviewers for their comments that improved the manuscript. Most of the figures are generated using the GMT software.

Appendix A. Supplementary data

Supplementary data to this article can be found online at https://doi.org/10.1016/j.jvolgeores.2018.04.004.

References

Acocella, V., Abebe, B., Korme, T., Barberi, F., 2008. Structure of Tendaho graben and Manda Hararo rift: implications for the evolution of the southern Red Sea propagator in Central Afar. Tectonics 27 (4).8.

Acton, G.D., Stein, S., Engeln, J.F., 1991. Block rotation and continental extension in Afar: a comparison to oceanic microplate systems. Tectonics 10 (3), 501–526.

Aiken, C., Peng, Z., 2014. Dynamic triggering of microearthquakes in three geothermal/volcanic regions of California. J. Geophys. Res. Solid Earth 119 (9), 6992–7009. https://doi.org/10.1002/2014JB011218. 2014JB011218.

Ali, S., Akerley, J., Baluyut, E., Cardiff, M., Davatzes, N., Feigl, K., Foxall, W., Fratta, D., Mellors, R., Spielman, P., Wang, H., Zemach, E., 2016. Time-series analysis of surface deformation at Brady Hot Springs geothermal field (Nevada) using interferometric synthetic aperture radar. Geothermics 61, 114–120. http://www.sciencedirect.com/science/article/pii/S0375650516000109.

Aquater, 1996. Tendaho geothermal project. Tech. Rep. MME, EIGS, Government of Italy-Ministry of Foreign Affairs.

Ayele, A., Ebinger, C.J., van Alstyne, C., Keir, D., Nixon, C.W., Belachew, M., Hammond, J.O.S., 2015. Seismicity of the central Afar rift and implications for Tendaho dam hazards. Geol. Soc. Lond., Spec. Publ. 420.

Ayele, A., Jacques, E., Kassim, M., Kidane, T., Omar, A., Tait, S., Nercessian, A., de Chabalier, J.-B., King, G., 2007. The volcano-seismic crisis in Afar, Ethiopia, starting September 2005. Earth Planet. Sci. Lett. 255 (1–2), 177–187.

Ayele, A., Keir, D., Ebinger, C., Keir, D., Wright, T.J., Stuart, G.W., Buck, W.R., Jacques, E., Ogubazghi, G., Sholan, J., 2009. September 2005 mega-dike emplacement in the Manda-Harraro nascent oceanic rift (Afar depression). Geophys. Res. Lett. 36 (L20306).

Battaglia, M., Troise, C., Obrizzo, F., Pingue, F., De Natale, G., 2006. Evidence for fluid migration as the source of deformation at Campi Flegrei caldera (Italy). Geophys. Res. Lett. 33 (1). https://doi.org/10.1029/2005GL024904. n/a-n/a, L01307.

Battistelli, A., Yiheyis, A., Calore, C., Ferragina, C., Abatneh, W., 2002. Reservoir engineering assessment of Dubti geothermal field, Northern Tendaho rift, Ethiopia. Geothermics 31 (3), 381–406.

Bekaert, D.P.S., Hooper, A., Wright, T.J., 2015. A spatially variable power law tropospheric correction technique for InSAR data. J. Geophys. Res. Solid Earth 120 (2), 1345–1356. 2.

Belachew, M., Ebinger, C., Coté, D., 2013. Source mechanisms of dike-induced earthquakes in the Dabbahu-Manda Hararo rift segment in Afar, Ethiopia: implications for faulting above dikes. Geophys. J. Int. 192, 907–917.

Belachew, M., Ebinger, C., Cotè, D., Keir, D., Rowland, J.V., Hammond, J.O.S., Ayele, A., 2011. Comparison of dike intrusions in an incipient seafloor-spreading segment in Afar, Ethiopia: seismicity perspectives. J. Geophys. Res. Solid Earth 116 (B6).

Berardino, P., Fornaro, G., Lanari, R., Sansosti, E., 2002. A new algorithm for surface deformation monitoring based on small baseline differential SAR interferograms. IEEE Trans. Geosci. Remote Sens. 40 (11), 2375–2383. 11.

Biggs, J., Anthony, E.Y., Ebinger, C.J., 2009. Multiple inflation and deflation events at Kenyan volcanoes, East African rift. Geology 37 (11), 979–982. Nov.

Biggs, J., Bastow, I.D., Keir, D., Lewi, E., 2011. Pulses of deformation reveal frequently recurring shallow magmatic activity beneath the main Ethiopian rift. Geochem. Geophys. Geosyst. 12 (9).

Biggs, J., Robertson, E., Cashman, K., 2016a. The lateral extent of volcanic interactions during unrest and eruption. Nat. Geosci. 9 (4), 308–311. Apr.

Biggs, J., Robertson, E., Cashman, K., 2016b. The lateral extent of volcanic interactions during unrest and eruption. Nat. Geosci. 9 (4), 308–311. https://doi.org/10.1038/ngeo2658. Feb, http://10.0.4.14/ngeo2658 https://www.nature.com/articles/ngeo2658#supplementary-information.

Biggs, J., Wright, T., Lu, Z., Parsons, B., 2007. Multi-interferogram method for measuring interseismic deformation: Denali Fault, Alaska. Geophys. J. Int. 170 (3), 1165–1179.

Bridges, D.L., Mickus, K., Gao, S.S., Abdelsalam, M.G., Alemu, A., 2012. Magnetic stripes of a transitional continental rift in Afar. Geology 40 (3), 203–206.

Bürgmann, R., Ayhan, M.E., Fielding, E.J., Wright, T.J., McClusky, S., Aktug, B., Demir, C., Lenk, O., Türkezer, A., 2002. Deformation during the 12 November 1999 Düzce, Turkey, earthquake, from GPS and InSAR data. Bull. Seismol. Soc. Am. 92 (1), 161–171. 2.

Cayol, V., Cornet, F.H., 1998. Effects of topography on the interpretation of the deformation field of prominent volcanoes–application to Etna. Geophys. Res. Lett. 25 (11), 1979–1982. https://doi.org/10.1029/98GL51512.

Chen, C.W., Zebker, H.A., 2000. Network approaches to two-dimensional phase unwrapping: intractability and two new algorithms. J. Opt. Soc. Am. A Opt. Image Sci. Vis. 17 (3), 401–414.

Didana, Y.L., Thiel, S., Heinson, G., 2014. Magnetotelluric imaging of upper crustal partial melt at Tendaho graben in Afar, Ethiopia. Geophys. Res. Lett. 41 (9), 3089–3095.

d'Oreye, N., Gonzalez, P.J., Shuler, A., Oth, A., Bagalwa, L., Ekstrom, G., Kavotha, D., Kervyn, F., Lucas, C., Lukaya, F., Osodundu, E., Wauthier, C., Fernandez, J., 2011. Source parameters of the 2008 Bukavu-Cyangugu earthquake estimated from InSAR and teleseismic data. Geophys. J. Int. 184 (2), 934–948.

Ebinger, C.J., Casey, M., 2001. Continental breakup in magmatic provinces: an Ethiopian example. Geology 29 (6), 527–530.

Elliott, J.R., Biggs, J., Parsons, B., Wright, T.J., 2008. InSAR slip rate determination on the Altyn Tagh fault, northern Tibet, in the presence of topographically correlated atmospheric delays. Geophys. Res. Lett. 35 (12).

Elliott, J.R., Walters, R.J., Wright, T.J., 2016. The role of space-based observation in understanding and responding to active tectonics and earthquakes. Nat. Commun. 7, 13844. http://10.0.4.14/ncomms13844. https://doi.org/10.1038/ncomms13844. Dec.

Farr, T.G., Kobrick, M., 2000. Shuttle radar topography mission produces a wealth of data. Eos. Trans. AGU 81 (48), 583. Nov.

Ferretti, A., Prati, C., Rocca, F., 2001. Permanent scatterers in SAR interferometry. IEEE Trans. Geosci. Remote Sens. 39 (1), 8–20. 1.

Fialko, Y., Simons, M., 2000. Deformation and seismicity in the Coso geothermal area, Inyo County, California: observations and modeling using satellite radar interferometry. J. Geophys. Res. Solid Earth 105 (B9), 21781–21793.

Galloway, D.L., Hudnut, K.W., Ingebritsen, S.E., Phillips, S.P., Peltzer, G., Rogez, F., Rosen, P.A., 1998. Detection of aquifer system compaction and land subsidence using interferometric synthetic aperture radar, Antelope Valley, Mojave Desert, California. Water Resour. Res. 34 (10), 2573. Oct.

Gaudio, C.D., Aquino, I., Ricciardi, G., Ricco, C., Scandone, R., 2010. Unrest episodes at Campi Flegrei: a reconstruction of vertical ground movements during 1905–2009. J. Volcanol. Geotherm. Res. 195 (1), 48–56. http://www.sciencedirect.com/science/article/pii/S0377027310001745.

Gianelli, G., Mekuria, N., Battaglia, S., Chersicla, A., Garofalo, P., Ruggieri, G., Manganelli, M., Gebregziabher, Z., 1998. Water-rock interaction and hydrothermal mineral equilibria in the Tendaho geothermal system. J. Volcanol. Geotherm. Res. 86 (1–4), 253–276. Nov.

Global Volcanism Program, 2013. Volcanoes of the World.

Goldstein, R.M., Werner, C.L., Kobrick, M., 1998. Radar Interferogram filtering for Geophysical applications. Geophys. Res. Lett. 25 (21), 4035–4038.

González, P.J., Bagnardi, M., Hooper, A.J., Larsen, Y., Marinkovic, P., Samsonov, S.V., Wright, T.J., 2015. The 2014–2015 eruption of Fogo volcano: geodetic modeling of Sentinel-1 TOPS interferometry. Geophys. Res. Lett. 42 (21), 9239–9246. 11.

González, P.J., Tiampo, K.F., Palano, M., Cannavó, F., Fernández, J., 2012. The 2011 Lorca earthquake slip distribution controlled by groundwater crustal unloading. Nat. Geosci. 5 (11), 821–825. Nov.

Gottsmann, J., Folch, A., Rymer, H., 2006a. Unrest at Campi Flegrei: a contribution to the magmatic versus hydrothermal debate from inverse and finite element modeling. J. Geophys. Res. Solid Earth 111 (B7). https://doi.org/10.1029/2005JB003745. n/a-n/a, B07203.

Gottsmann, J., Rymer, H., Berrino, G., 2006b. Unrest at the Campi Flegrei caldera (Italy): a critical evaluation of source parameters from geodetic data inversion. J. Volcanol. Geotherm. Res. 150 (1), 132–145. http://www.sciencedirect.com/science/article/pii/S037702730500257X. The Changing Shapes of Active Volcanoes.

Grandin, R., Socquet, A., Binet, R., Klinger, Y., Jacques, E., de Chabalier, J.-B., King, G.C.P., Lasserre, C., Tait, S., Tapponnier, P., Delorme, A., Pinzuti, P., 2009. September 2005 Manda Hararo-Dabbahu rifting event, Afar (Ethiopia): constraints provided by geodetic data. J. Geophys. Res. Solid Earth 114 (B8).

Grandin, R., Socquet, A., Doin, M.-P., Jacques, E., de Chabalier, J.-B., King, G.C.P., 2010. Transient rift opening in response to multiple dike injections in the Manda Hararo rift (Afar, Ethiopia) imaged by time-dependent elastic inversion of interferometric synthetic aperture radar data. J. Geophys. Res. Solid Earth 115 (B9).

Gresta, S., Patanè, D., Daniel, A., Zan, L., Carletti, A., Befekadu, O., 1997. Seismological evidence of active faulting in the Tendaho rift (Afar Triangle, Ethiopia). Pure Appl. Geophys. 149 (2), 357–374.

Hamling, I., Ayele, A., Bennati, L., Calais, E., Ebinger, C., Keir, D., Lewi, E., Wright, T., Yirgu, G., 2009. Geodetic observations of the ongoing Dabbahu rifting episode: new dyke intrusions in 2006 and 2007. Geophys. J. Int. 178, 989–1003.

Hamling, I.J., Hreinsdóttir, S., Clark, K., Elliott, J., Liang, C., Fielding, E., Litchfield, N., Villamor, P., Wallace, L., Wright, T.J., D'Anastasio, E., Bannister, S., Burbidge, D., Denys, P., Gentle, P., Howarth, J., Mueller, C., Palmer, N., Pearson, C., Power, W., Barnes, P., Barrell, D.J.A., Van Dissen, R., Langridge, R., Little, T., Nicol, A., Pettinga, J., Rowland, J., Stirling, M., 2017. Complex multifault rupture during the 2016 M_w 7.8 Kaikōura earthquake, New Zealand. Scienceeaam7194; Mar.

Hamling, I.J., Hreinsdóttir, S., Fournier, N., 2015. The ups and downs of the TVZ: geodetic observations of deformation around the Taupo Volcanic Zone, New Zealand. J. Geophys. Res. Solid Earth 120 (6), 4667–4679. https://doi.org/10.1002/2015JB012125. 2015JB012125.

Hamling, I.J., Wright, T.J., Calais, E., Bennati, L., Lewi, E., 2010. Stress transfer between thirteen successive dyke intrusions in Ethiopia. Nat. Geosci. 3 (10), 713–717. 10.

Hamling, I.J., Wright, T.J., Calais, E., Lewi, E., Fukahata, Y., 2014. InSAR observations of post-rifting deformation around the Dabbahu rift segment, Afar, Ethiopia. Geophys. J. Int. 197 (1), 33–49.

Hanssen, R.F., 2001. Radar Interferometry: Data Interpretation and Error Analysis. Kluwer Academic Publishers.

Hooper, A., 2008. A multi-temporal InSAR method incorporating both persistent scatterer and small baseline approaches. Geophys. Res. Lett. 35 (16).

Hooper, A., Pietrzak, J., Simons, W., Cui, H., Riva, R., Naeije, M., van Scheltinga, A.T., Schrama, E., Stelling, G., Socquet, A., 2013. Importance of horizontal seafloor motion on tsunami height for the 2011 Mw = 9.0 Tohoku-oki earthquake. Earth Planet. Sci. Lett. 361, 469–479.

Hussain, E., Wright, T.J., Walters, R.J., Bekaert, D., Hooper, A., Houseman, G.A., 2016. Geodetic observations of postseismic creep in the decade after the 1999 Izmit earthquake, Turkey: implications for a shallow slip deficit. J. Geophys. Res. B: Solid Earth 121 (4), 2980–3001. apr.

Hutchison, W., Biggs, J., Mather, T.A., Pyle, D.M., Lewi, E., Yirgu, G., Caliro, S., Chiodini, G., Clor, L.E., Fischer, T.P., 2016. Causes of unrest at silicic calderas in the East African Rift: new constraints from InSAR and soil-gas chemistry at Aluto volcano, Ethiopia. Geochem. Geophys. Geosyst. 17 (8), 3008–3030. https://doi.org/10.1002/2016GC006395.

Hutchison, W., Mather, T.A., Pyle, D.M., Biggs, J., Yirgu, G., 2015. Structural controls on fluid pathways in an active rift system: a case study of the Aluto volcanic complex. Geosphere 11 (3), 542–562.

Jackson, J., Bouchon, M., Fielding, E., Funning, G., Ghorashi, M., Hatzfeld, D., Nazari, H., Parsons, B., Priestley, K., Talebian, M., Tatar, M., Walker, R., Wright, T., 2006. Seismotectonic, rupture process, and earthquake-hazard aspects of the 2003 December 26 Bam, Iran, earthquake. Geophys. J. Int. 166 (3), 1270–1292.

Johnson, N.E., Whaler, K.A., Hautot, S., Fisseha, S., Desissa, M., Dawes, G.J.K., 2015. Magma imaged magnetotellurically beneath an active and an inactive magmatic segment in Afar, Ethiopia. Geol. Soc. Lond., Spec. Publ. 420.

Jolivet, R., Agram, P.S., Lin, N.Y., Simons, M., Doin, M.-P., Peltzer, G., Li, Z., 2014. Improving InSAR geodesy using global atmospheric models. J. Geophys. Res. Solid Earth 119 (3), 1–18.

Keir, D., Belachew, M., Ebinger, C.J., Kendall, J.-M., Hammond, J.O.S., Stuart, G.W., Ayele, A., Rowland, J.V., 2011. Mapping the evolving strain field during continental breakup from crustal anisotropy in the Afar depression. Nat. Commun. 2 (285).

Kidane, T., Courtillot, V., Manighetti, I., Audin, L., Lahitte, P., Quidelleur, X., Gillot, P.-Y., Gallet, Y., Carlut, J., Haile, T., 2003. New paleomagnetic and geochronologic results from Ethiopian Afar: block rotations linked to rift overlap and propagation and determination of a ~2 Ma reference pole for stable Africa. J. Geophys. Res. Solid Earth 108 (B2).

Kwoun, O.I., Lu, Z., Neal, C., Wicks, C., 2006. Quiescent deformation of the Aniakchak Caldera, Alaska mapped by InSAR. Geology 34 (1), 5–8.
Lanari, R., Berardino, P., Borgström, S., Gaudio, C.D., Martino, P.D., Fornaro, G., Guarino, S., Ricciardi, G., Sansosti, E., Lundgren, P., 2004. The use of IFSAR and classical geodetic techniques for caldera unrest episodes: application to the Campi Flegrei uplift event of 2000. J. Volcanol. Geotherm. Res. 133 (1), 247–260. http://www.sciencedirect.com/science/article/pii/S0377027303004013. The Neapolitan Volcanoes: Vesuvius, Campi Flegrei and Ischia.
Lanari, R., Casu, F., Manzo, M., Zeni, G., Berardino, P., Manunta, M., Pepe, A., 2007. An overview of the small baseline subset algorithm: a DInSAR technique for surface deformation analysis. Pure Appl. Geophys. 164 (4), 637–661.
Lewi, E., Keir, D., Birhanu, Y., Blundy, J., Stuart, G., Wright, T., Calais, E., 2015. Use of a high-precision gravity survey to understand the formation of oceanic crust and the role of melt at the southern Red Sea rift in Afar, Ethiopia. Geol. Soc. Lond., Spec. Publ. 420.
Lisowski, M., 2007. Analytical volcano deformation source models. Volcano Deformation. Springer, Berlin, Heidelberg, pp. 279–304.
Lockner, D.A., Beeler, N.M., 1999. Premonitory slip and tidal triggering of earthquakes. J. Geophys. Res. Solid Earth 104 (B9), 20133–20151. Sep.
Lu, Z., Dzurisin, D., Biggs, J., Wicks, C., McNutt, S., 2010. Ground surface deformation patterns, magma supply, and magma storage at Okmok Volcano, Alaska, from InSAR analysis: 1. Intereruption deformation, 1997–2008. J. Geophys. Res. Solid Earth 115 (5).B00B02; May.
Lu, Z., Fielding, E., Patrick, M.R., Trautwein, C.M., 2003. Estimating lava volume by precision combination of multiple baseline spaceborne and airborne interferometric synthetic aperture radar: the 1997 eruption of Okmok volcano, Alaska. IEEE Trans. Geosci. Remote Sens. 41 (6), 1428–1436. 6.
Manconi, A., Walter, T.R., Amelung, F., 2007. Effects of mechanical layering on volcano deformation. Geophys. J. Int. 170 (2), 952–958. https://doi.org/10.1111/j.1365-246X.2007.03449.x.
Massonnet, D., Feigl, K.L., 1998. Radar interferometry and its application to changes in the Earth's surface. Rev. Geophys. 36 (4), 441. https://doi.org/10.1029/97RG03139. Nov.
Masterlark, T., 2007. Magma intrusion and deformation predictions: sensitivities to the Mogi assumptions. J. Geophys. Res. Solid Earth 112 (B6). https://doi.org/10.1029/2006JB004860. n/a-n/a, B06419.
McClusky, S., Reilinger, R., Ogubazghi, G., Amleson, A., Healeb, B., Vernant, P., Sholan, J., Fisseha, S., Asfaw, L., Bendick, R., Kogan, L., 2010. Kinematics of the southern Red Sea-Afar Triple Junction and implications for plate dynamics. Geophys. Res. Lett. 37 (5).3.
Mogi, K., 1958. Relations between the eruptions of various volcanoes and the deformations of the ground surfaces around them. Bull. Earthquake Res. Inst. 36, 99–134.
Mosegaard, K., Tarantola, A., 1995. Monte Carlo sampling of solutions to inverse problems. J. Geophys. Res. Solid Earth 100 (B7), 12431–12447. 7.
Okada, Y., 1985. Surface deformation due to shear and tensile faults in a half-space. Bull. Seismol. Soc. Am. 75 (4), 1135–1154. 8.
Pagli, C., Wang, H., Wright, T.J., Calais, E., Lewi, E., 2014. Current plate boundary deformation of the Afar rift from a 3-D velocity field inversion of InSAR and GPS. J. Geophys. Res. Solid Earth 119 (11), 8562–8575. 11.
Parker, A.L., Biggs, J., Walters, R.J., Ebmeier, S.K., Wright, T.J., Teanby, N.A., Lu, Z., 2015. Systematic assessment of atmospheric uncertainties for InSAR data at volcanic arcs using large-scale atmospheric models: application to the cascade volcanoes, United States. Remote Sens. Environ. 170, 102–114. http://www.sciencedirect.com/science/article/pii/S0034425715301267.
Pritchard, M.E., Jay, J.A., Aron, F., Henderson, S.T., Lara, L.E., 2013. Subsidence at southern Andes volcanoes induced by the 2010 Maule, Chile earthquake. Nat. Geosci. 6 (8), 632–636. https://doi.org/10.1038/ngeo1855. July, http://10.0.4.14/ngeo1855 https://www.nature.com/articles/ngeo1855#supplementary-information.
Rigden, W.G., 1981. Afar, Ethiopia: A Local Seismic Survey.(Ph.D. thesis). Durham University.
Robertson, E.A.M., Biggs, J., Cashman, K.V., Floyd, M.A., Vye-Brown, C., 2016. Influence of regional tectonics and pre-existing structures on the formation of elliptical calderas in the Kenyan Rift. Geol. Soc. Lond., Spec. Publ. 420 (1), 43–67. https://doi.org/10.1144/SP420.12. Sept.
Rosen, P.A., Hensley, S., Peltzer, G., Simons, M., 2004. Updated repeat orbit interferometry package released. Eos Trans. AGU 85 (5), 47.
Rosen, P.A., Hensley, S., Zebker, H.A., Webb, F.H., Fielding, E.J., 1996. Surface deformation and coherence measurements of Kilauea Volcano, Hawaii, from SIR-C radar interferometry. J. Geophys. Res. Planets 101 (E10), 23109–23125.
Samsonov, S., van der Kooij, M., Tiampo, K., 2011. A simultaneous inversion for deformation rates and topographic errors of DInSAR data utilizing linear least square inversion technique. Comput. Geosci. 37 (8), 1083–1091.
Sanderson, R., Johnson, J., Lees, J., 2010. Ultra-long period seismic signals and cyclic deflation coincident with eruptions at Santiaguito volcano, Guatemala. J. Volcanol. Geotherm. Res. 198 (1), 35–44. http://www.sciencedirect.com/science/article/pii/S0377027310002532.
Shevenell, L., Oppliger, G., Coolbaugh, M., Faulds, J., 2012. Bradys (Nevada) InSAR anomaly evaluated with historical well temperature and pressure data. Transactions - Geothermal Resources Council. vol. 36 2. pp. 1383–1390. Reno, NV.
Simons, M., Rosen, P.A., 2015. Interferometric synthetic aperture radar geodesy. In: Schubert, G. (Ed.), Treatise on Geophysics. vol. 3. Oxford, Elsevier, pp. 339–385.
Stiros, S.C., Psimoulis, P., Vougioukalakis, G., Fyticas, M., 2010. Geodetic evidence and modeling of a slow, small-scale inflation episode in the Thera (Santorini) volcano caldera, Aegean Sea. Tectonophysics 494 (3), 180–190. http://www.sciencedirect.com/science/article/pii/S0040195110003653.
Takada, Y., Fukushima, Y., 2014. Volcanic subsidence triggered by the 2011 Tohoku earthquake in Japan: hot and weak material hypothesis. Nat. Geosci. 16, 4056. https://www.nature.com/articles/ngeo1857#supplementary-information. https://doi.org/10.1038/ngeo1857. jul.
Tapponnier, P., Armijo, R., Manighetti, I., Courtillot, V., 1990. Bookshelf faulting and horizontal block rotations between overlapping rifts in southern Afar. Geophys. Res. Lett. 17 (1), 1–4. https://doi.org/10.1029/GL017i001p00001.
Vasco, D.W., Rutqvist, J., Ferretti, A., Rucci, A., Bellotti, F., Dobson, P., Oldenburg, C., Garcia, J., Walters, M., Hartline, C., 2013. Monitoring deformation at the Geysers Geothermal Field, California using C-band and X-band interferometric synthetic aperture radar. Geophys. Res. Lett. 40 (11), 2567–2572. https://doi.org/10.1002/grl.50314.
Vasco, D.W., Wicks, C., Karasaki, K., Marques, O., 2002. Geodetic imaging: reservoir monitoring using satellite interferometry. Geophys. J. Int. 149 (3), 555–571.
Vilardo, G., Isaia, R., Ventura, G., De Martino, P., Terranova, C., 2010. InSAR permanent scatterer analysis reveals fault re-activation during inflation and deflation episodes at Campi Flegrei caldera. Remote Sens. Environ. 114 (10), 2373–2383.
Walter, T.R., 2007. How a tectonic earthquake may wake up volcanoes: Stress transfer during the 1996 earthquake-eruption sequence at the Karymsky Volcanic Group, Kamchatka. Earth Planet. Sci. Lett. 264 (3–4), 347–359. Dec.
Wang, H., 2012. PI-RATE. http://homepages.see.leeds.ac.uk/earhw/software/pirate/index.html.
Wang, H., Wright, T.J., 2012. Satellite geodetic imaging reveals internal deformation of western Tibet. Geophys. Res. Lett. 39 (7).4.
Wang, H., Wright, T.J., Biggs, J., 2009. Interseismic slip rate of the northwestern Xianshuihe fault from InSAR data. Geophys. Res. Lett. 36 (3).
Wang, H., Wright, T.J., Yu, Y., Lin, H., Jiang, L., Li, C., Qiu, G., 2012. InSAR reveals coastal subsidence in the Pearl River Delta China. Geophys. J. Int. 191 (3), 1119–1128.
Wright, T.J., Ebinger, C., Biggs, J., Ayele, A., Yirgu, G., Keir, D., Stock, A., 2006. Magma-maintained rift segmentation at continental rupture in the 2005 Afar dyking episode. Nature 442, 291–294.
Wright, T.J., Lu, Z., Wicks, C., 2003. Source model for the Mw 6.7, 23 October 2002, Nenana Mountain Earthquake (Alaska) from InSAR. Geophys. Res. Lett. 30 (18).
Xu, W., Jónsson, S., 2015. Birth of two volcanic islands in the southern Red Sea. Nat. Commun. 6.
Zandbergen, R., Otten, M., Righetti, P.L., Kuijper, D., Dow, J.M., 2003. Integrated space geodetic systems and satellite dynamics routine operational and high-precision orbit determination of Envisat. Adv. Space Res. 31 (8), 1953–1958.